

Article

Microstructure Modulation of Zn Doped VO₂(B) Nanorods with Improved Electrochemical Properties towards High Performance Aqueous Batteries

Dewei Liu, Qijie Zhang, Xiaohong Chen, Haiyang Dai, Xuezhen Zhai, Jing Chen, Gaoshang Gong, Cui Shang and Xuzhe Wang * 

Laboratory of Magnetoelectronic Information, School of Physics and Electronic Engineering, Henan Key Functional Materials, Zhengzhou University of Light Industry, Zhengzhou 450002, China

* Correspondence: xuzhewang@zzuli.edu.cn; Tel.: +86-371-86608910

Abstract: Vanadium dioxide with monoclinic structure is theoretically a promising layered cathode material for aqueous metal-ion batteries due to its excellent specific capacity. However, its poor cycling stability limits its application as an electrode material. In this study, a series of Zn-doped VO₂ (V_{1-x}ZnxO₂) nanorods were successfully fabricated by the technology of one-step hydrothermal synthesis. The XRD result indicated that there was a slight lattice distortion caused by doped Zn²⁺ with a larger ion radius. The positron lifetime spectrum showed that there were vacancy cluster defects in all the samples. The electrochemical measurement demonstrated the enhancement of the specific capacitance of V_{1-x}ZnxO₂ electrodes compared with the undoped sample. In addition, the discharge capacitance of the sample remained around 86% after 1000 charge/discharge cycles. This work proves that Zn²⁺ doping is a valid tactic for the application of nano-VO₂(B) in energy storage electrode materials.



Citation: Liu, D.; Zhang, Q.; Chen, X.; Dai, H.; Zhai, X.; Chen, J.; Gong, G.; Shang, C.; Wang, X. Microstructure Modulation of Zn Doped VO₂(B) Nanorods with Improved Electrochemical Properties towards High Performance Aqueous Batteries. *Batteries* **2022**, *8*, 172. <https://doi.org/10.3390/batteries8100172>

Academic Editor: Carlos Zieber

Received: 6 September 2022

Accepted: 29 September 2022

Published: 9 October 2022

Publisher's Note: MDPI stays neutral with regard to jurisdictional claims in published maps and institutional affiliations.



Copyright: © 2022 by the authors. Licensee MDPI, Basel, Switzerland. This article is an open access article distributed under the terms and conditions of the Creative Commons Attribution (CC BY) license (<https://creativecommons.org/licenses/by/4.0/>).

Keywords: vanadium dioxide; Zn doping; positron annihilation technique; microstructures; electrochemical properties

1. Introduction

The rising demands for batteries in electric vehicles are driving the development of new energy conversion and storage technologies based on new materials with better overall electrochemical properties [1–3]. The next-generation aqueous metal-ion batteries, of high safety, low cost and high theoretical specific capacitance, are considered as promising candidates for the future energy storage applications [4,5]. The cathode materials, as the most important component affecting the performance of aqueous metal-ion batteries, remain the biggest bottleneck restricting their further practical applications.

The vanadium-based compounds have been widely used as electrode materials because of their high specific capacity and fast ion diffusion kinetics for aqueous metal-ion batteries, which arise from various chemical valences of V^{x+} ($x = 3, 4, 5$) and large interlayer spacing [6–8]. Particularly, monoclinic phase VO₂(B) consists of two identical angular VO₆ octahedrons superimposed along the B-axis, and it has a tunnel structure which is beneficial to metal ion embedding and de-embedding. In addition, the edge-sharing VO₆ octahedron endows the metastable monoclinic VO₂(B) with layered structural flexibility alleviating severe structural distortion during the extraction and insertion of metal ions in electrolytes during the electrochemical reaction process. It has been reported that the V₂O₅·xH₂O xerogel cathode exhibits an initial capacity of 308 mAh·g⁻¹ at 1.0–4.0 V [9]. A reversible capacity of about 200 mAh·g⁻¹ can be achieved at 50 mA·g⁻¹ in metal-ion batteries between 1.5 and 4.0 V [10]. However, the VO₂(B) electrode materials still face a severe capacitance fading problem in practical applications [11]. This may be related to the interface reaction between the vanadium and electrolyte in the process of acid–base

interaction, which aggravates the dissolution problem of $\text{VO}_2(\text{B})$ [12]. As a result, the loss of active materials can trigger the fast capacity fade caused by the catalytic decomposition of the electrolyte. This problem has been a serious obstacle for the development of $\text{VO}_2(\text{B})$ electrode materials.

The electrode materials are the critical factors determining the cyclability of aqueous metal-ion batteries, and some of the literature has reported that doping with metal cations can effectively enhance the structural stability and cyclability of cathode materials [13,14]. It has been reported that a $\text{Co}_{0.16}\text{Zn}_{0.09}\text{V}_2\text{O}_5 \cdot n\text{H}_2\text{O}$ electrode exhibits an initial capacity of $90 \text{ mAh} \cdot \text{g}^{-1}$ at $3.0 \text{ A} \cdot \text{g}^{-1}$, and the capacitance retention is 97% after 1000 cycles [15]. In our previous study, Mn ion-doped $\text{VO}_2(\text{B})$ was used as the electrode of aqueous metal-ion batteries with enhanced electrochemical performance [16]. It is still necessary, however, to verify the mechanism behind the enhancement of stability and cyclability by the metal cation doping process for aqueous metal-ion batteries.

The electrochemical properties of the $\text{VO}_2(\text{B})$ material are closely associated with its microstructures and internal defects. The effects of vacancy defects in $\text{VO}_2(\text{B})$ material on the energy bands, phase-transition characteristics and electronic structure were studied by Wang and Cui based on first principles [17,18]. The computational results showed that vacancy defects were related to the local density of electronic states, which could introduce electrons as free carriers and narrow the energy band gap of the $\text{VO}_2(\text{B})$ cathode material. The positron annihilation technique is highly sensitive and efficient at detecting the evolution of defects in solid materials. It can particularly detect the local electron density and vacancy defects in materials [19].

In this study, considering that the ionic radius of Zn^{2+} (0.74 \AA) is relatively approximate to that of V^{4+} (0.58 \AA), doping with the Zn ion can create defects and improve the rate capability [20]. Thus, the $\text{V}_{1-x}\text{Zn}_x\text{O}_2$ samples with different Zn ion doping concentrations were fabricated, and the effect of Zn^{2+} -doping on the microstructure and electrochemical performances of $\text{V}_{1-x}\text{Zn}_x\text{O}_2$ samples was researched. The experimental results indicated that the doped Zn ion could increase the lattice binding volume of $\text{V}_{1-x}\text{Zn}_x\text{O}_2$ samples and introduce large-sized vacancy defects, thereby improving the electrochemical properties of the cathode material for aqueous metal-ion batteries.

2. Experiment

2.1. Preparation of $\text{V}_{1-x}\text{Zn}_x\text{O}_2$ Samples

$\text{V}_{1-x}\text{Zn}_x\text{O}_2$ samples ($0.000 \leq x \leq 0.030$) were prepared by a simple hydrothermal synthesis method. All raw materials were employed immediately without further purification. A moderate vanadium pentoxide (V_2O_5) with a purity of 99.99% was blended in oxalic acid ($\text{H}_2\text{C}_2\text{O}_4$) with a purity of 99.0% at a concentration ratio of 1:3 and stirred for 0.5 h in a magnetic agitator. A specific stoichiometric ratio of zinc nitrate nonahydrate ($\text{Zn}(\text{NO}_3)_2 \cdot 9\text{H}_2\text{O}$, 99.99%) as the doping source was added into a mixture of deionized water and hydrogen peroxide (H_2O_2 , 30.0%) and stirred in a magnetic stirrer for 0.5 h. The two resulting mixtures were combined and stirred in a magnetic mixer for 1.5 h to form the mixed liquor. Then, the final mixed liquor was removed to a 250 mL Teflon-packaged stainless steel reaction vessel and stored at 180°C for 50 h. The precipitation was cleaned six times alternately with anhydrous ethanol and deionized water. Finally, the resulting $\text{V}_{1-x}\text{Zn}_x\text{O}_2$ nanorods were procured by heating at 80°C for 15 h in a vacuum oven.

2.2. Characterization of $\text{V}_{1-x}\text{Zn}_x\text{O}_2$ Samples

The determination of the phase structures of the $\text{V}_{1-x}\text{Zn}_x\text{O}_2$ samples was performed by X-ray powder diffraction (XRD, SmartLab SE, Cu-K α radiation, $\lambda = 1.5418 \text{ \AA}$) within a 2θ scope of 10° – 80° with a scan step of 0.02° . The Le Bail method was used to obtain the lattice parameters and mean crystallite size. The microstructure of the samples was analyzed via scanning electron microscopy (FESEM, JSM-7001F) and high-resolution transmission electron microscopy (HRTEM, JSM2100). The positron annihilation lifetime spectra of the samples were studied via fast-fast coincidence lifetime spectrometer, and ^{22}Na was used as

the positron radiation source with a strength of approximately 13 μCi . A PATFIT program was employed to analyze the lifetime spectrum of the samples.

2.3. Electrochemical Measurements

The electrochemical performance of $\text{V}_{1-x}\text{Zn}_x\text{O}_2$ electrodes was investigated using a CHI760E electrochemical workstation in 2 mol/L KOH aqueous solution at room temperature. The $\text{V}_{1-x}\text{Zn}_x\text{O}_2$ electrodes were produced by mixing the synthesized nanorods, acetylene black and polytetrafluoroethylene with a quantity ratio of 8:1:1 in anhydrous ethanol. Afterwards, the hybrid paste was evenly coated on a kiln-dried nickel foam plate and vacuum-dried at 80 °C for 12 h for the succeeding measurement. The electrochemical performance was evaluated by the three-electrode test method: the prepared $\text{V}_{1-x}\text{Zn}_x\text{O}_2$ electrode served as the working electrode and the platinum electrode and calomel electrode were employed as counter electrode and reference electrode, respectively [21]. The cyclic voltammetry (CV), galvanostatic charge–discharge (GCD) and electrochemical impedance spectroscopy (EIS) of the $\text{V}_{1-x}\text{Zn}_x\text{O}_2$ electrodes were measured.

3. Results and Discussion

3.1. Structural Characterizations

The atomic ratio of zinc, vanadium and oxide in the $\text{V}_{1-x}\text{Zn}_x\text{O}_2$ with different doping concentrations was calculated according to the XPS spectra. As shown in Figure 1, the actual amounts of zinc are slightly less than the calculated amounts in the fabrication process, which means that not all the zinc ion in the precursor solution could be doped into the $\text{VO}_2(\text{B})$. The XRD patterns of the $\text{V}_{1-x}\text{Zn}_x\text{O}_2$ ($x = 0.000, 0.005, 0.015, 0.030$) samples are shown in Figure 2a. All the diffraction peaks of the samples are related to the monoclinic crystal structure of $\text{VO}_2(\text{B})$ with the space group $C2/m$ (PDF No. 31-1438), and there is no obvious trace of an impurity phase in the samples. The XRD patterns show that the crystalline grains of all $\text{V}_{1-x}\text{Zn}_x\text{O}_2$ samples germinated preferentially along the (110) orientation. Figure 2b shows an enlarged image of the (110) peaks of the XRD patterns. It is clear that the (110) peaks of the XRD pattern gradually shifted to the lower degree with the increase in Zn ion doping amounts. This may be due to the lattice expansion caused by the replacement of V^{4+} (0.58 Å) by Zn^{2+} (0.74 Å) with a larger radius. However, for the (002) and (−401) peaks in the inset of Figure 2b, little shift can be observed. This phenomenon can be ascribed to the lattice distortion of the (110) crystal plane caused by the doping process. In addition, the relative intensities of the peaks show a drop which may be caused by the decrease in crystalline degree with the doping concentration increased. The noticeable decrease in (001) and (002) can be ascribed to the inhibiting effect on the (001) and (002) crystallographic plane of the doping ion into the crystalline structure of $\text{VO}_2(\text{B})$. The lattice parameters and unit cell volumes of the $\text{V}_{1-x}\text{Zn}_x\text{O}_2$ samples were obtained by the Le Bail method and are shown in Table 1. It can be noted that the unit cell volumes of the doped $\text{V}_{1-x}\text{Zn}_x\text{O}_2$ samples became larger than that of the undoped sample; this may be attributed to the increase in the lattice parameters a and c . The calculated lattice parameters show small and random variations, which can be attributed to the fact that the doping concentration was too low to cause a regular change in the lattice parameters. The results show that the Zn^{2+} doping with a larger radius led to the expansion of the crystalline structure, which may have benefited the electrochemical performance of the $\text{V}_{1-x}\text{Zn}_x\text{O}_2$ samples.

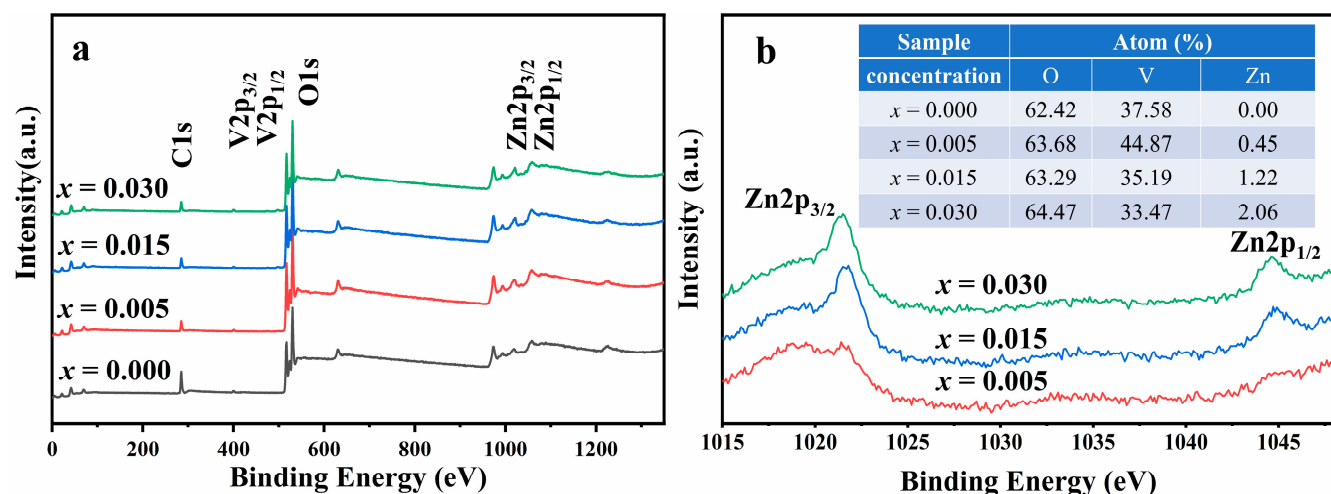


Figure 1. (a) XPS spectra of $\text{V}_{1-x}\text{Zn}_x\text{O}_2$ samples; (b) XPS spectra of Zn 2p_{3/2} and Zn 2p_{1/2}; the inset of (b) is the atomic ratio of oxide, vanadium and zinc.

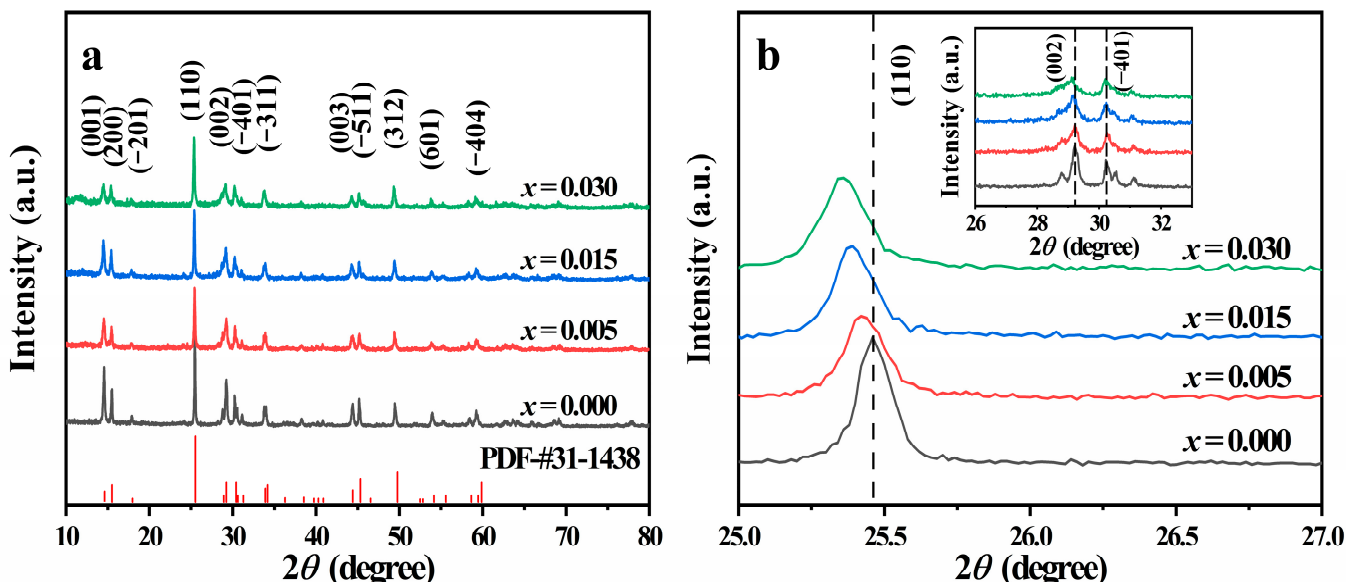


Figure 2. (a) XRD patterns of $\text{V}_{1-x}\text{Zn}_x\text{O}_2$ samples; (b) the enlarged view of (110) peaks of the XRD patterns; the inset of (b) is the enlarged view of (002) and (-401) peaks.

Table 1. The calculated lattice constants and cell volumes of the $\text{V}_{1-x}\text{Zn}_x\text{O}_2$ samples.

| Doping Concentration | Lattice Parameters | | | | β | |
|----------------------|--------------------|---------|---------|---------|---------|---------|
| | x | a (Å) | b (Å) | c (Å) | | |
| 0.000 | | 12.0707 | 3.6958 | 6.4270 | 274.23 | 106.966 |
| 0.005 | | 12.0801 | 3.6943 | 6.4411 | 275.02 | 106.909 |
| 0.015 | | 12.0759 | 3.6981 | 6.4319 | 274.81 | 106.906 |
| 0.030 | | 12.0842 | 3.6925 | 6.4552 | 275.57 | 106.912 |

Figure 3 shows the SEM pictures of the $\text{V}_{1-x}\text{Zn}_x\text{O}_2$ samples. The surface morphologies of all the $\text{V}_{1-x}\text{Zn}_x\text{O}_2$ samples are nanorods. The average grain size of the $\text{V}_{1-x}\text{Zn}_x\text{O}_2$ samples is between 60 nm and 240 nm. For the $x = 0.000, 0.005, 0.015$ and 0.030 samples, the average diameters are 133.8 nm, 122.6 nm, 120.6 nm and 101.6 nm, respectively. Notably, the average diameter decreases with increasing doping Zn ion concentrations, which means

that the doped Zn^{2+} with larger radius may have an inhibitory effect on the growth of $V_{1-x}Zn_xO_2$ nanorods.

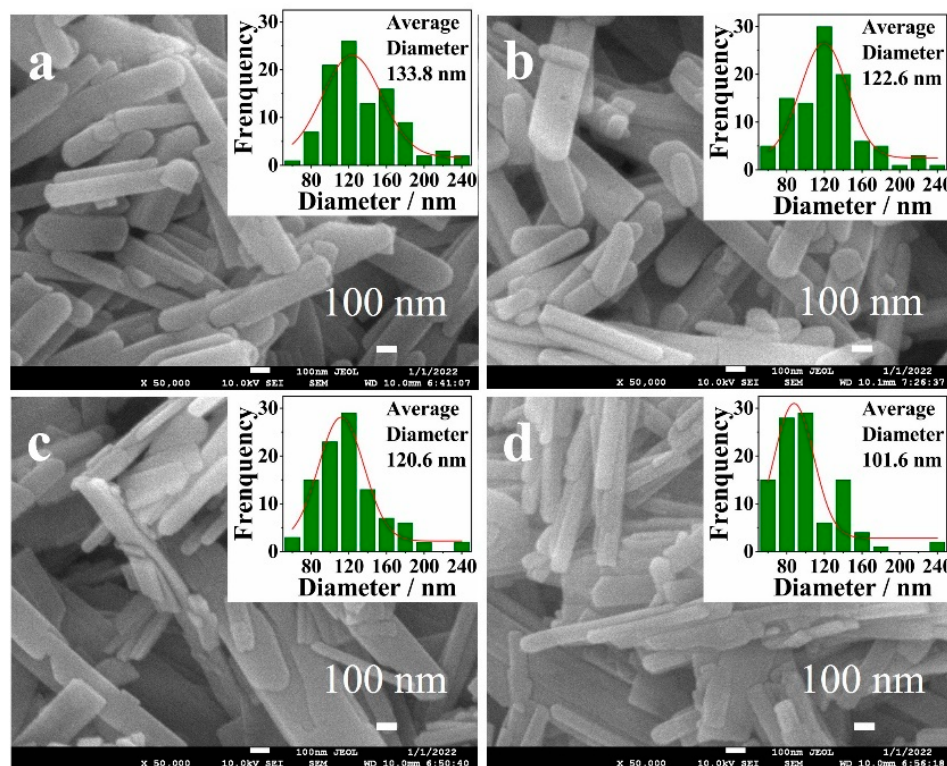


Figure 3. SEM images of $V_{1-x}Zn_xO_2$ samples: (a) $x = 0.000$; (b) $x = 0.005$; (c) $x = 0.015$; (d) $x = 0.030$.

The crystal structure of the prepared samples can be further analyzed by TEM. Figure 4 shows the TEM images of $V_{1-x}Zn_xO_2$ samples with the doping concentrations of 0.000, 0.005 and 0.015. It can be seen from Figure 4a–c that there is no distinct change in the structure and morphology of the samples after Zn ion doping. Compared with the undoped sample, the doped samples maintain the morphology of nanorods with diameters of about 80–200 nm. This is consistent with the SEM images of Figure 3. In addition, the lattice fringes can be seen clearly in Figure 4d–f, and the high-resolution TEM images display the distances of 0.248 nm, 0.506 nm and 0.312 nm, corresponding to the interplanar distance of the (-402) , (-201) and (-202) planes, respectively, which indicate good crystallinity for all samples. The results are consistent with the XRD analysis results in Figure 2 and Table 1.

The lifetime parameters of the positron annihilation of the $V_{1-x}Zn_xO_2$ samples were analyzed by the PATFIT program. The different types of the defects in the samples had different local electron densities, and so corresponded to different positron annihilation lifetimes τ . The relative strength I of the lifetime constituent represented the corresponding concentration of the defects in the materials.

The short lifetime component τ_1 is commonly attributed to the positron annihilation in surface states. The long lifetime component τ_2 is related to the positron annihilation of defect regions and denotes the size of defects in samples. The intensity I_2 reflects the concentration of defects in the samples [22]. As shown in Figure 5, when the doping concentration x of the Zn ion increases from 0.000 to 0.005, the value of τ_2 increases linearly. However, when the Zn ion concentration rises from 0.005 to 0.030, the value of τ_2 reduces gradually. This phenomenon is caused by the competition between the low-valence Zn ion doping effect and the large-radius Zn ion doping effect on the positron lifetime [23]. To be specific, the larger-radius ion doping will increase the defect size, while the low-valence ion doping will lead to a decrease in the vacancy defect size. When the doping amount of Zn ions is between 0.000 and 0.005, the larger-radius effect is the main factor in determining

the defect size. When the doping amount of Zn ions is between 0.005 and 0.015, the low-valence effect is the main factor in determining the defect size. In summary, under the joint modulation of the larger-radius effect and the low-valence effect, the size of defects in the $V_{1-x}Zn_xO_2$ samples increase initially and decrease afterwards with the increase in the Zn doping amount.

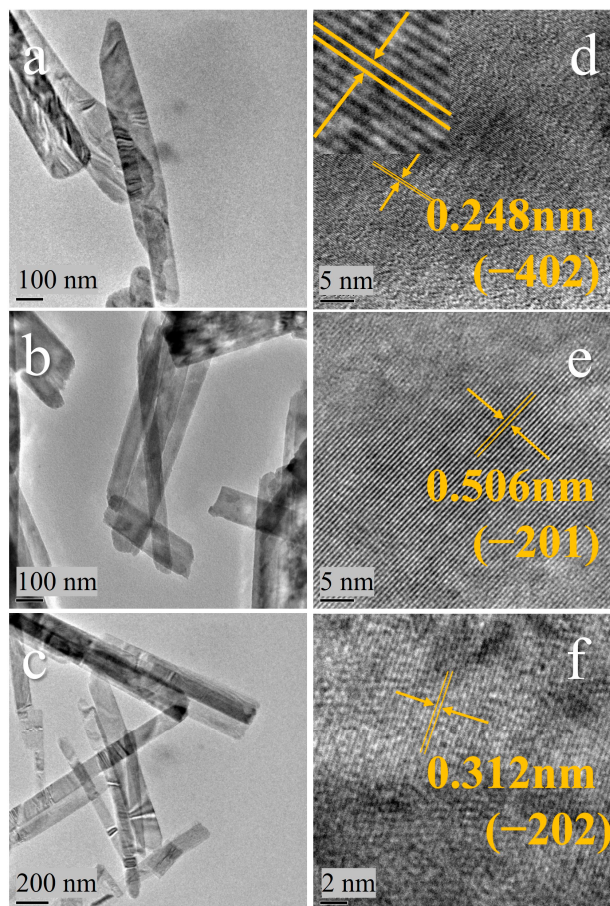


Figure 4. TEM and HRTEM images of $V_{1-x}Zn_xO_2$ samples: (a) and (d) $x = 0.000$; (b) and (e) $x = 0.005$; (c) and (f) $x = 0.015$; the inset of (d) is an enlarged view of the lattice fringes.

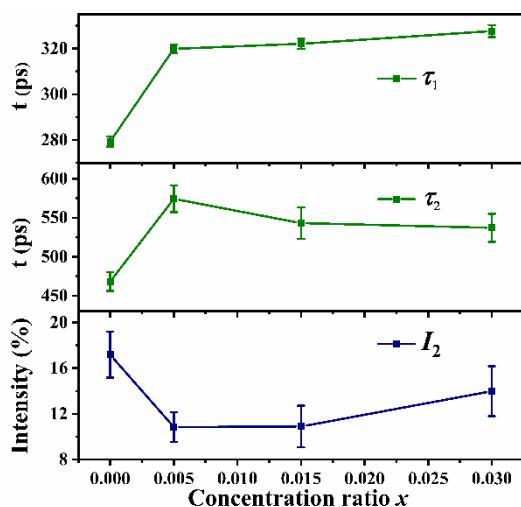


Figure 5. The positron lifetime parameters τ_1 , τ_2 and I_2 of $V_{1-x}Zn_xO_2$ samples.

The positron bulk lifetime (τ_b) reflects the local electron density in the crystal lattice and can be computed according to the formula derived from the two-state trapping model [24]:

$$\tau_b = 1/(I_1/\tau_1 + I_2/\tau_2)$$

Table 2 shows the positron lifetime values τ_1 , τ_2 , τ_b , τ_m , I_1 and I_2 of the $V_{1-x}Zn_xO_2$ samples. The types of defects are judged by the ratio of τ_2/τ_b . When the ratio of τ_2/τ_b is in the range of 1.1–1.3, 1.3–1.4, and >1.5, it represents single vacancy, double vacancy and vacancy clusters, respectively [22]. The computed τ_2/τ_b values are 1.56, 1.71, 1.61 and 1.55 for $x = 0.000$, 0.005 , 0.015 and 0.030 samples, respectively, indicating that vacancy clusters are present in all $V_{1-x}Zn_xO_2$ samples. The mean lifetime τ_m can be computed according to the formula:

$$\tau_m = \tau_1 \times I_1 + \tau_2 \times I_2$$

Table 2. The positron lifetime values τ_1 , I_1 , τ_2 , I_2 , τ_b and τ_m of $V_{1-x}Zn_xO_2$ samples.

| Sample | Positron Lifetime/ps | | Intensity/% | | Bulk Lifetime/ps | Mean Lifetime/ps |
|--------|----------------------|----------|-------------|---------|------------------|------------------|
| x | τ_1 | τ_2 | I_1 | I_2 | τ_b | τ_m |
| 0.000 | 279.4 | 468.4 | 82.8177 | 17.1823 | 300.2141 | 311.8745 |
| 0.005 | 319.9 | 574.2 | 89.1532 | 10.8468 | 336.0428 | 347.4834 |
| 0.015 | 322.1 | 543.1 | 89.1115 | 10.8885 | 337.0332 | 346.1636 |
| 0.030 | 327.7 | 537.2 | 86.0118 | 13.9882 | 346.6081 | 357.0053 |

This reflects the process of positron annihilation in free states and trap states, and gives detailed information on the electron density and defect distribution inside the material [25]. The τ_m values of the experimental samples are shown in Table 2. Compared with the undoped $VO_2(B)$ sample, the τ_m of those doped samples becomes significantly larger. This reflects the fact that Zn doping leads to a decrease in the electron density of the vacancy defects and annihilation sites in the lattices, which can be considered as a variation of the chemical environment around the annihilation states.

3.2. Electrochemical Performance

The potential applications of $V_{1-x}Zn_xO_2$ samples in electrochemical performance were further investigated by the cyclic voltammetry (CV), electrochemical impedance spectroscopy (EIS) and galvanostatic charge–discharge (GCD) in a three-electrode system. The CV curves of $V_{1-x}Zn_xO_2$ at a scanning rate of 100 mV / s are shown in Figure 6a. The two kinds of peaks, reduction peaks and oxidation peaks, can be seen clearly for all the samples in the CV curves, indicating the electrode process battery behavior. The good reversibility and structural stability of the $V_{1-x}Zn_xO_2$ electrode can be proved by the symmetrical shape of the CV curves, which indicates the stable (de)intercalation of metal ion in the electrode materials [26–28].

As shown in Figure 6b, according to the GCD curves at a current density of $0.1\text{ A}\cdot\text{g}^{-1}$, the slopes in the voltage range of 0.52 V–0.44 V and 0.32 V–0.20 V are larger, while the slopes in the range of 0.44 V–0.32 V are clearly gentler. When x increases from 0 to 0.015, the discharge time gradually increases, and as x increases to 0.030, the charge and discharge time decreases, and the $x = 0.015$ sample possesses the best charge–discharge performance.

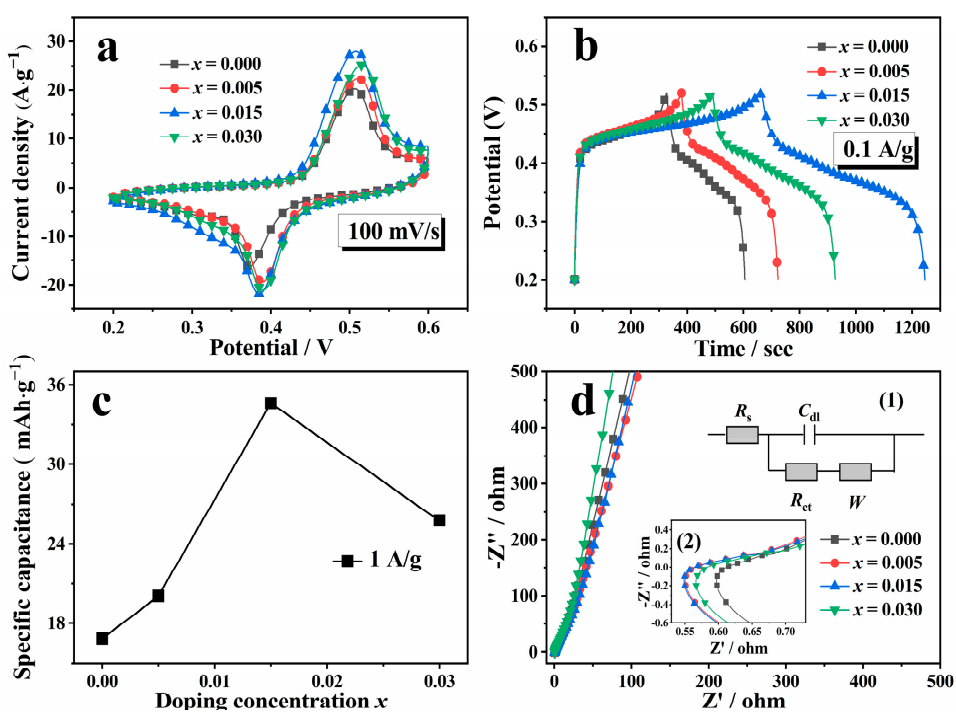


Figure 6. Electrochemical measurements of $V_{1-x}Zn_xO_2$ samples: (a) CV curves at different doping concentrations; (b) Potential vs. time for charge-discharge profiles of all samples at 0.1 A/g; (c) Specific capacitance of samples with different doping concentrations; (d) Nyquist plots curves.

According to the galvanostatic discharge curves, the specific capacitance (C) of electrodes can be calculated by the following equation:

$$C = \frac{I}{m} \cdot \left(\frac{\Delta t}{3.6} \right)$$

where I (A) represents the load current; m (g) shows the quality of active materials; Δt (s) represents the discharge time [29,30]. As can be seen from Figure 6c, with an increase in Zn ion-doping concentrations, the calculated specific capacitance of the prepared samples firstly increases and then decreases under the same current density. Compared with the $VO_2(B)$ electrode, the specific capacitance performance of the Zn-doped samples is significantly enhanced. In particular, the sample of $x = 0.015$ possesses the highest specific capacity.

As the most important indicator to evaluate electrochemical performance, the integrated electrochemical impedance spectroscopy (EIS) is used to judge the electrode conductivity, charge transfer performance and diffusion property [31]. The Nyquist plot for $V_{1-x}Zn_xO_2$ electrodes within the frequency range of 10^{-2} – 10^5 Hz is shown in Figure 6d. The inset (1) of Figure 6d shows the simulated equivalent circuit, where R_s denotes the electrolyte resistance, R_{ct} indicates the resistance of charge transfer between the electrolyte and electrode, C_{dl} shows the double-layer capacitor representing the contact electrode surface and W shows the Warburg impedance [32,33]. In the low frequency range, there is no significant difference in the slopes of the impedance curves for all samples. As shown in the inset (2) of Figure 6d, the intersection points of the impedance curve with the x axis signify the ohmic resistance between the electrolyte and the surface of the electrode materials. It is obvious that the doped samples possess lower resistance. When the doping amount x is 0.015, the resistance is the lowest, indicating the highest electrochemical activity, which is in accord with the CV and GCD results.

According to the above electrochemical results, it can be seen that the $V_{1-x}Zn_xO_2$ ($x = 0.015$) sample has the best electrochemical performance. In order to further explore

the enhancement mechanism of the electrochemical activity behind the doping process, we conducted more detailed electrochemical measurements on the $V_{1-x}Zn_xO_2$ ($x = 0.015$) sample. The CV curves at different scan rates are illustrated in Figure 7a, from which we can see that the potential window increases with the increase in the scan rate, but still maintains a similar shape. These phenomena can be ascribed to the excellent amplification performance of the $V_{1-x}Zn_xO_2$ ($x = 0.015$) electrode. Figure 7b demonstrates the CV curves at 100 mV/s for 1000 cycles. The peak shape of the CV curves has good repeatability after 1000 cycles. This indicates that $V_{1-x}Zn_xO_2$ ($x = 0.015$) still maintains good cycling stability. Figure 7c shows the GCD curves of $V_{1-x}Zn_xO_2$ ($x = 0.015$) electrode at different current densities. The GCD curves exhibit the behavioral features of a supercapacitor, which are primarily attributed to the quasi-reversible redox reactions or electrochemical desorption/adsorption on the electrode contact surface in the electrolyte. In addition, it can be seen in Figure 7d that the capacitance retention is 88% after 1000 cycles. This means the $V_{1-x}Zn_xO_2$ ($x = 0.015$) electrode possesses excellent cycling durability, which may be caused by its crystalline structural stability. The electrochemical performance of the $V_{1-x}Zn_xO_2$ ($x = 0.015$) electrode indicates its potential application as electrodes for energy storage devices.

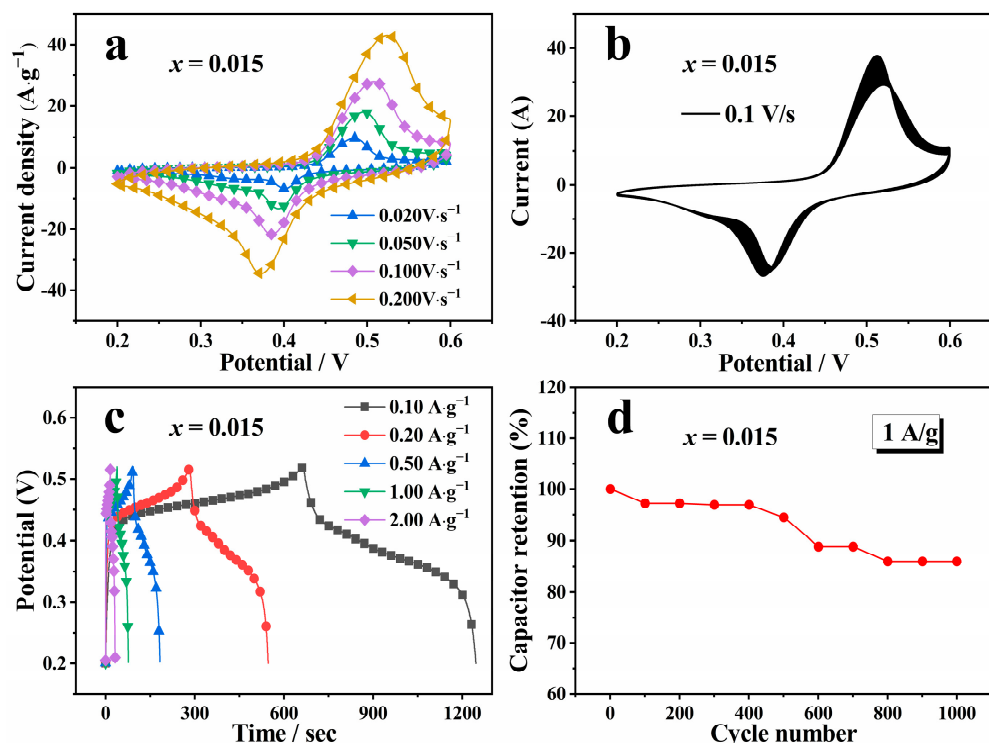


Figure 7. Electrochemical measurement of $V_{1-x}Zn_xO_2$ samples with $x = 0.015$: (a) CV curves at different scan rates; (b) the CV curves after 1000 cycles at a scan rate of 100 mV/s; (c) galvanostatic discharge profiles at different current density; (d) cycling performance at $1\text{ A}\cdot\text{g}^{-1}$.

4. Conclusions

In summary, the influence of Zn ion-doping on the crystalline structure, morphologies and defect formation has carefully explored. The potential applications on electrochemical performance have also been studied. The doping process can cause the lattice expansion in the unit cell volume. SEM and TEM images indicate that all the prepared samples are well-crystallized nanorods. The results of positron lifetime spectroscopy confirm that Zn ion-doping can introduce large vacancy clusters. Electrochemical measurements demonstrate that the electrochemical performance of $V_{1-x}Zn_xO_2$ samples can be enhanced by doped Zn ions. This work can provide an effective protocol for the fabrication of advanced electrode materials with optimized performance.

Author Contributions: Conceptualization, D.L., X.Z. and X.W.; Formal analysis, Q.Z. and X.C.; Funding acquisition, D.L., H.D., X.Z., J.C., G.G. and C.S.; Project administration, D.L. and X.W.; Supervision, D.L., H.D., X.Z., J.C., G.G., C.S. and X.W.; Writing—original draft, Q.Z.; Writing—review and editing, D.L. and X.W. All authors have read and agreed to the published version of the manuscript.

Funding: This work was funded by the National Natural Science Foundation of China (Grant Nos. 12005194, 11804311, 11775192, 11405148), the Key Research & Development and promotion projects in Henan Province (Grant Nos. 212102210132, 212102210477, 212300410092, 222102230101) and the postgraduate education reform and quality improvement projects in Henan Province (Grant Nos. HNYJS2021AL027, DWJZW202131zn).

Institutional Review Board Statement: Not applicable.

Informed Consent Statement: Not applicable.

Data Availability Statement: Not applicable.

Conflicts of Interest: The authors declare no conflict of interest.

References

1. Bella, F.; Griffini, G.; Correa, J.P.; Saracco, G.; Gratzel, M.; Hagfeldt, A.; Turri, S.; Gerbaldi, C. Improving efficiency and stability of perovskite solar cells with photocurable fluoropolymers. *Science* **2016**, *354*, 203–206. [[CrossRef](#)] [[PubMed](#)]
2. Yang, Z.G.; Zhang, J.L.; Kintner-Meyer, M.C.W.; Lu, X.C.; Choi, D.W.; Lemmon, J.P.; Liu, J. Electrochemical energy storage for green grid. *Chem. Rev.* **2011**, *111*, 3577–3613. [[CrossRef](#)] [[PubMed](#)]
3. Huie, M.M.; Bock, D.C.; Takeuchi, E.S.; Marschilok, A.C.; Takeuchi, K.J. Cathode materials for magnesium and magnesium-ion based batteries. *Coord. Chem. Rev.* **2015**, *287*, 15–27.
4. Liu, Q.; Hu, Z.; Zhang, Y.; Xing, G.; Tang, Y.; Chou, S. Designing Advanced Vanadium-Based Materials to Achieve Electrochemically Active Multielectron Reactions in Sodium/Potassium-Ion Batteries. *Adv. Energy Mater.* **2020**, *10*, 2002244.
5. Liu, J.; Xu, C.; Chen, Z.; Ni, S.; Shen, Z. Progress in aqueous rechargeable batteries. *Green Energy Environ.* **2018**, *3*, 20–41. [[CrossRef](#)]
6. Chen, X.; Wang, L.; Li, H.; Cheng, F.; Chen, J. Porous V₂O₅ nanofibers as cathode materials for rechargeable aqueous zinc-ion batteries. *J. Energy Chem.* **2019**, *38*, 20–25. [[CrossRef](#)]
7. Zhang, Y.; Chen, A.; Sun, J. Promise and challenge of vanadium-based cathodes for aqueous Zinc-ion batteries. *J. Energy Chem.* **2021**, *54*, 655–667. [[CrossRef](#)]
8. Wan, F.; Niu, Z. Design Strategies for Vanadium-based Aqueous Zinc-Ion Batteries. *Angew. Chem. Int. Ed.* **2019**, *58*, 16358–16367. [[CrossRef](#)]
9. Wei, Q.; Liu, J.; Feng, W.; Sheng, J.; Tian, X.; He, L.; An, Q.; Mai, L. Hydrated vanadium pentoxide with superior sodium storage capacity. *J. Mater. Chem. A* **2015**, *3*, 8070. [[CrossRef](#)]
10. Wang, W.; Jiang, B.; Hu, L.; Lin, Z.; Hou, J.; Jiao, S. Single crystalline VO₂ nanosheets: A cathode material for sodium-ion batteries with high rate cycling performance. *J. Power Source* **2014**, *250*, 181. [[CrossRef](#)]
11. Liu, Y.; Wu, X. Review of vanadium-based electrode materials for rechargeable aqueous zinc ion batteries. *J. Energy Chem.* **2021**, *56*, 223–237. [[CrossRef](#)]
12. Zhao, Q.; Jiao, L.; Peng, W.; Gao, H.; Yang, J.; Wang, Q.; Du, H.; Li, L.; Qi, Z.; Si, Y.; et al. Facile synthesis of VO₂(B)/carbon nanobelts with high capacity and good cyclability. *J. Power Source* **2012**, *199*, 350–354. [[CrossRef](#)]
13. Wang, F.; Liu, Y.; Liu, C.Y. Hydrothermal synthesis of carbon/vanadium dioxide core-shell microspheres with good cycling performance in both organic and aqueous electrolytes. *Electrochim. Acta* **2010**, *55*, 2662–2666. [[CrossRef](#)]
14. Liu, G.; Du, Y.; Liu, W.; Wen, L. Study on the action mechanism of doping transitional elements in spinel LiNi_{0.5}Mn_{1.5}O₄. *Electrochim. Acta* **2016**, *209*, 308–314. [[CrossRef](#)]
15. Huang, H.; Tian, T.; Pan, L.; Chen, X.; Tervoort, E.; Shih, C.J.; Niederberger, M. Layered metal vanadates with different interlayer cations for high-rate Na-ion storage. *J. Mater. Chem. A* **2019**, *7*, 16109. [[CrossRef](#)]
16. Liu, D.; Zhang, Q.; Ding, S.; Yan, F.; Dai, H.; Li, T.; Xue, R.; Chen, J.; Gong, G.; Shang, C.; et al. Microdefects evolution and electrochemical performance modulation of Mn doped VO₂(B) nanorods. *J. Alloys Compd.* **2022**, *911*, 164975. [[CrossRef](#)]
17. Fang, D.L.; Li, J.C.; Liu, X.; Huang, P.F.; Xu, T.R.; Qian, M.C.; Zheng, C.H. Synthesis of a Co-Ni doped LiMn₂O₄ spinel cathode material for high-power Li-ion batteries by a sol-gel mediated solid-state route. *J. Alloys Compd.* **2015**, *640*, 82–89. [[CrossRef](#)]
18. Akkila, T.; Mansur Basha, I. Study of structural, morphological and optical properties of nano-structured zinc doped V₂O₅ thin films. *J. Pure Appl. Sci. Technol.* **2018**, *8*, 18–33.
19. Cui, Y.Y.; Liu, B.; Chen, L.L.; Luo, H.J.; Gao, Y.F. Formation energies of intrinsic point defects in monoclinic VO₂ studied by first-principles calculations. *AIP Adv.* **2016**, *6*, 105301–105309. [[CrossRef](#)]
20. Wang, X.; Wang, Z.; Zhang, G.; Jiang, J. Insight into electronic and structural reorganizations for defect-induced VO₂ metal-insulator transition. *J. Phys. Chem. Lett.* **2017**, *8*, 3129–3132. [[CrossRef](#)]

21. Kumar, N.S.; Chang, J.H.; Ho, M.-S.; Balraj, B.; Chandrasekar, S.; Mohanbabu, B.; Gowtham, M.; Guo, D.; Mohanraj, K. Impact of Zn²⁺ Doping on the Structural, Morphological and Photodiode Properties of V₂O₅ Nanorods. *J. Inorg. Organomet. Polym. Mater.* **2020**, *31*, 1066–1078. [[CrossRef](#)]
22. Dai, H.; Ye, F.; Chen, Z.; Li, T.; Liu, D. The effect of ion doping at different sites on the structure, defects and multiferroic properties of BiFeO₃ ceramics. *J. Alloys Compd.* **2018**, *734*, 60–65. [[CrossRef](#)]
23. Qi, X.; Dho, J.; Tomov, R.; Blamire, M.G.; MacManus-Driscoll, J.L. Greatly reduced leakage current and conduction mechanism in aliovalent-ion-doped BiFeO₃. *Appl. Phys. Lett.* **2005**, *86*, 062903. [[CrossRef](#)]
24. Puska, M.J.; Nieminen, R.M. Theory of positrons in solids and on solid surfaces. *Rev. Mod. Phys.* **1994**, *66*, 841. [[CrossRef](#)]
25. Wang, M.; Dai, H.; Li, T.; Chen, J.; Yan, F.; Xue, R.; Xing, X.; Chen, D.; Ping, T.; He, J. The evolution of structure and properties in GdMn_(1-x)Ti_xO₃ ceramics. *J. Mater. Sci. Mater. Electron.* **2021**, *32*, 27348–27361. [[CrossRef](#)]
26. Wang, H.; Wang, M.; Tang, Y. A novel zinc-ion hybrid supercapacitor for long-life and low-cost energy storage applications. *Energy Storage Mater.* **2018**, *13*, 1–7. [[CrossRef](#)]
27. Wu, X.; Tao, Y.; Dong, L.; Wang, Z.; Hu, Z. Preparation of VO₂ nanowires and their electric characterization. *Mater. Res. Bull.* **2005**, *40*, 315–321. [[CrossRef](#)]
28. Li, N.; Huang, W.; Shi, Q.; Zhang, Y.; Song, L. A CTAB-assisted hydrothermal synthesis of VO₂ (B) nanostructures for lithium-ion battery application. *Ceram. Int.* **2013**, *39*, 6199–6206. [[CrossRef](#)]
29. Wang, X.; Xi, B.; Ma, X.; Feng, Z.; Jia, Y.; Feng, J.; Qian, Y.; Xiong, S. Boosting Zinc-Ion Storage Capability by Effectively Suppressing Vanadium Dissolution Based on Robust Layered Barium Vanadate. *Nano Lett.* **2020**, *20*, 2899–2906. [[CrossRef](#)]
30. Ma, Y.; Zhu, X.; Wang, B.; Liu, S.; Meng, T.; Chen, H.; Peng, B.; Deng, Z. Sacrificial template synthesis of hierarchical nickel hydroxidenitrate hollow colloidal particles for electrochemical energy storage. *Chem. Eng. Sci.* **2020**, *217*, 115548. [[CrossRef](#)]
31. Yang, H.; Cheng, Z.; Wu, P.; Wei, Y.; Jiang, J.; Xu, Q. Deep eutectic solvents regulation synthesis of multi-metal oxalate for electrocatalytic oxygen evolution reaction and supercapacitor applications. *Electrochim. Acta* **2022**, *427*, 140879. [[CrossRef](#)]
32. Mahadi, N.B.; Park, J.S.; Park, J.H.; Chung, K.Y.; Yi, S.Y.; Sun, Y.K.; Myung, S.T. Vanadium dioxide-reduced graphene oxide composite as cathode materials for rechargeable Li and Na batteries. *J. Power Source* **2016**, *326*, 522–532. [[CrossRef](#)]
33. Liu, Q.; Tan, G.Q.; Wang, P.; Abeyweera, S.C.; Zhang, D.T.; Rong, Y.C.; Wu, Y.A.; Lu, J.; Sun, C.J.; Ren, Y.; et al. Revealing mechanism responsible for structural reversibility of single-crystal VO₂ nanorods upon lithiation/delithiation. *Nano Energy* **2017**, *36*, 197–205. [[CrossRef](#)]